Appl. Phys. B (2013) 112:539–545
DOI 10.1007/s00340-013-5436-z

Applied Physics B
Lasers and Optics

Synthesis and characterization of aligned ZnO/MgO core–shell nanorod arrays on ITO substrate

M. Gao · J. H. Yang · L. L. Yang · Y. J. Zhang · H. L. Liu · H. G. Fan · J. H. Lang · Y. R. Sui · B. Feng · Y. F. Sun · Z. Q. Zhang · H. Song

Received: 24 December 2012 / Accepted: 21 March 2013 / Published online: 9 April 2013

Abstract ZnO/MgO core–shell nanorod arrays were synthesized successfully by the hydrothermal growth method. Photoluminescence (PL) emission from the nanorods showed remarkable enhancement after the growth of the MgO layer. The ZnO/MgO core–shell nanorods are type-I heterostructures, the electrons and holes of which are both confined in the core of the nanorods, as a result, leading to the increase of the photoluminescence intensity in this system. In addition, another reason for the enhancement of PL emission was the deposition of MgO shell suppression of surface defects. In addition, the activation energy (E_a) of 63 meV in the ZnO/MgO core–shell nanorods was obtained from temperature-dependent PL.

M. Gao · B. Feng · Y. F. Sun · H. Song
Key Laboratory of Excited State Processes, Changchun Institute of Optics, Fine Mechanics and Physics, Chinese Academy of Sciences, South Nanhu Street No. 3888, Changchun 130033, People's Republic of China

M. Gao · B. Feng · Y. F. Sun
Graduate School of the Chinese Academy of Sciences, Sanlihe Road No. 52, Beijing 100049, People's Republic of China

M. Gao · J. H. Yang (✉) · L. L. Yang · Y. J. Zhang · H. L. Liu · H. G. Fan · J. H. Lang · Y. R. Sui · B. Feng · Y. F. Sun · Z. Q. Zhang
Key Laboratory of Functional Materials Physics and Chemistry of the Ministry of Education, Institute of Condensed State Physics, Jilin Normal University, Haifeng Street No. 1301, Siping 136000, People's Republic of China
e-mail: jhyang1@jlnu.edu.cn

1 Introduction

ZnO is a wide-bandgap (3.37 eV) semiconducting material with good chemical stability, making it useful in solar cells, light emitting diodes, gas sensing devices and transistors [1–3]. In the field of nanotechnology the synthesis of controllable structures is crucial for the development of functional devices. Recent interest in the nanostructures has boosted the design of nanoscale materials with specific morphologies for novel device applications, since it is known that physical and chemical properties of materials are strongly influenced by their size and shape [4, 5]. Recently, many ZnO nanorod devices have been reported to be fabricated by the facile and low-temperature (below 100 °C) hydrothermal methods [6, 7]. But this low-temperature chemical growth method will introduce high defect density, it may be disadvantageous to passivate the surface of the nanorods to control the surface reactivity and limit the electronic influence of surface defects [8]. It is reported that a common technique to control and enhance the properties of nanostructures is to create core–shell heterostructures [9, 10]. As a typical wide-bandgap insulator, MgO has drawn special attention due to its important use as a passivation layer in the study of chemical sensors, optical devices and superconductor products [11, 12]. Previously, MgO as a shell onto a metal oxide semiconducting core was developed using high-temperature synthesis routes [13]. But these methods are incompatible with low-cost, easily reproducible and large industrial scale fabrication of products.

Here we report a low-temperature (with the entire synthesis being possible under 100 °C), simple and efficient two-step fabrication process to fabricate ZnO nanorods inner- and MgO outer-shell layers. We comparatively

investigated the ZnO nanorods and ZnO/MgO core–shell nanorods with respect to their structural and photoluminescence (PL) characteristics.

2 Experimental

2.1 Nanorods core–shell synthesis

ZnO/MgO core–shell nanorods were grown by hydrothermal growth methods by a two-step process: growth of ZnO nanorods, MgO deposition on the ZnO nanorods. (1) Before growth of ZnO nanorods, the indium tin oxide (ITO) substrates were cleaned in acetone and following standard substrate cleaning procedures in a cleanroom environment. A solution of zinc acetate dihydrate [$Zn(OOCCH_3)_2{\cdot}2H_2O$] dissolved in pure ethanol with concentration of 5 mM was spin-coated on the substrate as the seed layer. In the chemical bath deposition (CBD) growth, the aqueous solutions of zinc nitrate hexahydrate [$Zn(NO_3)_2{\cdot}6H_2O$, 99.9 % purity] and methenamine ($C_6H_{12}N_4$, 99.9 % purity) were prepared and mixed together. The concentration of both solutions was fixed at 0.1 M. The pretreated ITO substrates were immersed into the aqueous solution and ZnO was grown at 95 °C. More details on controllable preparation process of ZnO nanorods and other controllable growth conditions can be found elsewhere [14]. To guarantee comparability, a big piece of sample was cut into two parts. One was used as as-grown sample; the other was used to deposit MgO shell. (2) The ZnO/MgO core–shell nanorod arrays were fabricated by a second hydrothermal growth procedure. The initial ZnO nanorods were submerged in a mixed solution of 10 mM magnesium nitrate and 0.1 M NaOH at 98.5 °C for 40 min in a water bath for constant temperature. After being taken out of the solution and washed with deionized water, the samples were dried on a hot plate at 100 °C to remove any excess water.

2.2 Characterization

XRD (MAC Science, MXP18, Japan), SEM (Hitachi, S-570), Raman spectroscopy (514.5 nm, argon ion laser, Renishaw-inVia) and PL (325 nm, He–Cd Laser, Renishaw-inVia) were used to characterize the crystal structure, surface morphology and optical properties of the samples.

3 Results and discussion

Figure 1 shows the X-ray diffraction (XRD) patterns for the initial ZnO nanorods and ZnO/MgO core–shell nanorod arrays. The peaks of the initial ZnO nanorods can be indexed to a hexagonal wurtzite ZnO structure with no other phase (Fig. 1a). In the case of ZnO/MgO core–shell nanorod arrays, the XRD pattern (Fig. 1b) shows a coexistence of ZnO and MgO phases, indicating that MgO was coated on the ZnO nanorods. The strongest (002) diffraction peak appearing in both XRD patterns indicated that the nanorods are preferentially oriented in the *c*-axis direction, which indicates that the ZnO nanorods tend to grow perpendicular to the substrate surface. Moreover, we can observe that the (002) peak position slightly shifts from 34.7° to 34.91° due to the MgO coating on the ZnO nanorods. The two-theta values of (002) XRD peaks from ZnO/MgO nanorods were shifted approximately 0.21° towards the bigger angle as compared with that from the as-prepared ZnO nanorods. We believe, in our case, this shift is mainly caused by the change of the stress due to the MgO deposition on the ZnO nanorod core. To prove this deduction, we calculated the stress in as-prepared ZnO nanorods and ZnO/MgO core–shell nanorods by the following formula [15]:

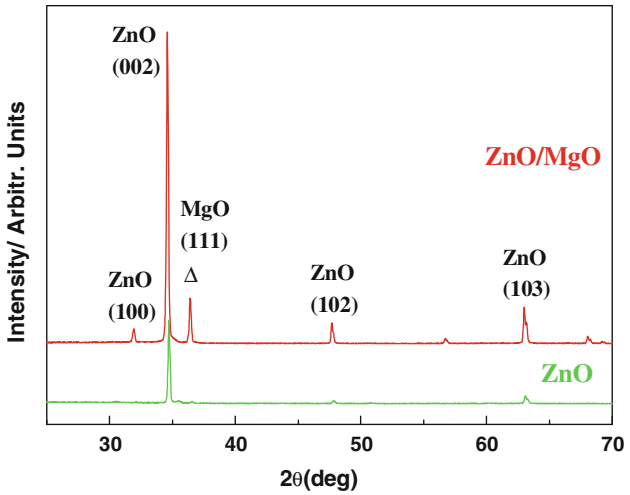

Fig. 1 XRD pattern of as-synthesized ZnO and ZnO/MgO core–shell nanorod arrays samples

$$\sigma = 450\,(C_0 - C)/C_0 \text{GPa} \quad (1)$$

where σ, C and C_0 were the mean stress, lattice constant, and lattice constant of bulk ZnO (standard $C_0 =$ 0.5209 nm). The calculated stress for the as-prepared ZnO nanorods and ZnO/MgO core–shell nanorods were 0.43 and 2.24, respectively, indicating that the compressive strain in ZnO increased with the deposition of MgO shell.

The typical SEM images of as-prepared ZnO nanorods are shown in Fig. 2a, showing the long-range uniformity and relative high density of our nanorod films. The ZnO nanorods are approximately 1 μm long and 300 nm in diameter. The clear hexagonal shape and smooth surface as shown in Fig. 2b revealed the high quality of the nanorods.

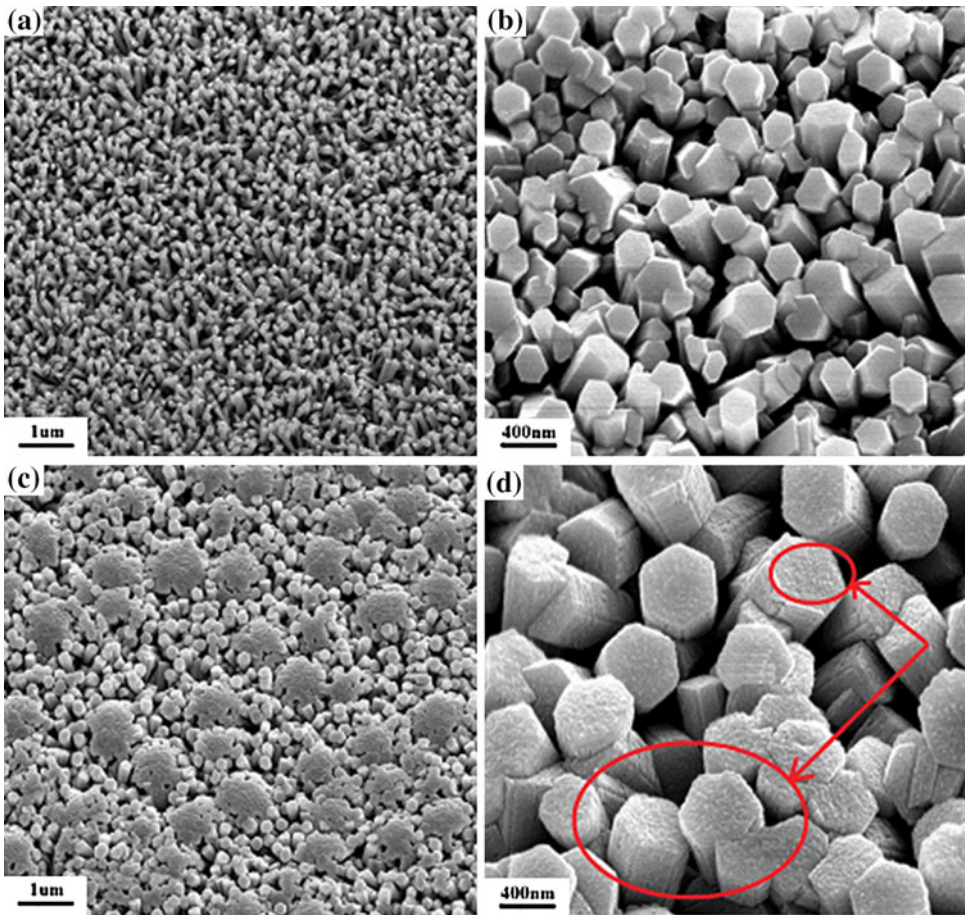

Fig. 2 **a** Typical SEM image of the initial ZnO nanorods; **b** high-magnified SEM image of ZnO nanorods; **c** SEM image of ZnO/MgO core–shell nanorod arrays; **d** high-magnified SEM image of ZnO/MgO core–shell nanorod arrays

Figure 2c shows that the SEM image of the converted ZnO/MgO core–shell nanorods seems to have bigger diameter of about 400 nm. Figure 2d demonstrates that MgO nanoparticles with a size of ~40 nm are successfully deposited onto the surface of ZnO nanorods.

The room-temperature Raman spectra were taken with 514.5 nm beam of Ar^+ laser to obtain the information about the local bonding configuration of as-prepared ZnO nanorods and ZnO/MgO core–shell nanorods. Group theory predicts the typical wurtzite ZnO zone centered optical phonons, $\Gamma = A_1 + 2B_1 + E_1 + 2E_2$, where B_1 mode is silent and A_1, E_1, and E_2 modes are Raman active. In addition, the A_1 and E_1 modes are polar and infrared active, and thus split into transverse-optical (TO) and longitudinal-optical (LO) phonons. The E_2 mode consists of two modes of low- and high-frequency phonons [16]. As shown in Fig. 3a, the Raman peak at 439 cm^{-1} is attributed to the ZnO nonpolar optical phonons of E_{2H} mode, which is one of the characteristic peaks of wurtzite ZnO. In comparison to as-prepared ZnO nanorods, one of the most interesting changes is that the intensity of E_{2H} mode of ZnO/MgO core–shell nanorod arrays is much higher than the initial ZnO nanorods, which maybe due to the very high density of surface defects in ZnO nanorods grown by low-temperature chemical method. However, in ZnO/MgO core–shell nanorods, the MgO shell passivates ZnO core surface and effectively reduces the density of surface states, thereby enabling the detection of enhanced Raman signals. The bands at 331, 381, 581, and 663 cm^{-1} can be assigned to the overtone of E_{2H}–E_{2L}, A_{1T}, E_{1L} and $3E_{2H}$–E_{2L}, respectively [16]. The room-temperature resonance Raman spectra of as-prepared ZnO nanorods and ZnO/MgO core–shell nanorods are shown in Fig. 3b. A He–Cd laser (3.82 eV) higher than the band gap of ZnO (3.37 eV) was used as the excitation source. It satisfies the incoming resonant conditions, where the exciting photon energy resonates with the interband electronic transition energy of the wurtzite ZnO. Therefore, the A_{1L} and E_{1L} phonon of ZnO multiphonon resonant Raman scattering can be observed. But in ZnO nanorods grown on the ITO substrate in the excitation geometry parallel to the *c*-axis of ZnO, the photon scattered by the E_{1L} phonon is forbidden according to the selection rule; hence, the corresponding Raman peak cannot be observed. As a result, when excited by He–Cd 325 nm laser beam, A_{1L} phonons outside the Brillouin zone center are activated leading to multiple overtone scattering. The peak intensity increases and the width broadens after the MgO deposition on the ZnO nanorod core. This implies

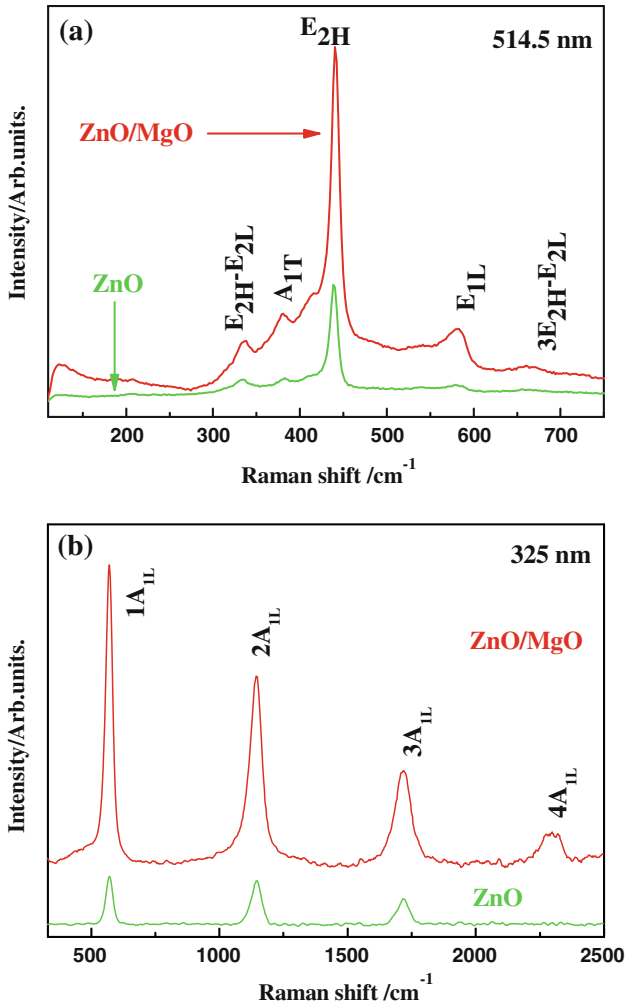

Fig. 3 Raman spectrum of the initial ZnO nanorods and ZnO/MgO core–shell nanorod arrays: **a** excited with 514.5 nm beam of Ar^+ laser; **b** excited with 325 nm beam of He–Cd laser

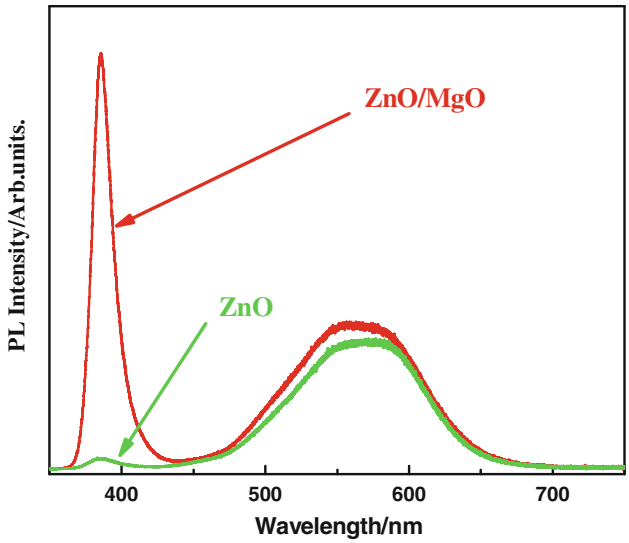

Fig. 4 PL spectra of the initial ZnO nanorods and ZnO/MgO core–shell nanorod arrays at room temperature

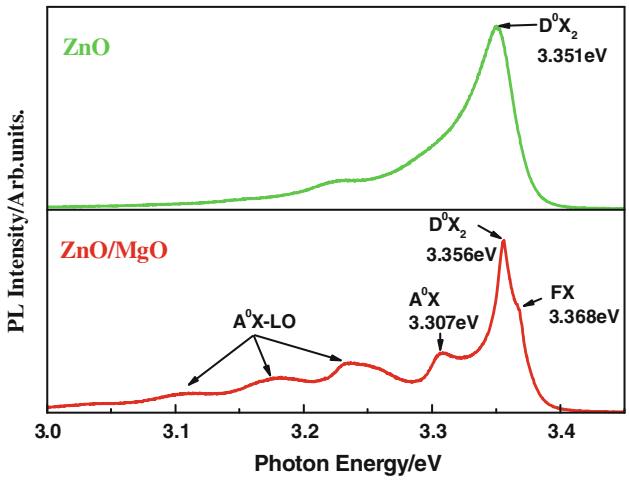

Fig. 5 PL spectra of **a** the initial ZnO nanorods at 80 K; **b** ZnO/MgO core–shell nanorod arrays at 80 K

that the MgO shell effectively reduces the density of surface states and forms a bigger average diameter compared with ZnO nanorods, which is consistent with the previously mentioned normal Raman results.

Optical investigations can reveal very useful information for understanding the physical properties of materials. They also demonstrate the possibility of extending the potential application of ZnO/MgO core–shell nanorod arrays in optoelectronic devices. Therefore, the PL measurement was performed at both room temperature and low temperature with an excitation wavelength of 325 nm. Figure 4 shows the room-temperature PL spectra of the initial ZnO nanorods and ZnO/MgO core–shell nanorods. The PL spectrum of the as-prepared ZnO nanorods consists of the near band edge (NBE) emission located at 385 and the deep level emission (DLE) in the green range centered at 566 nm [17]. The DLE band is mainly attributed to the intrinsic defects, such as oxygen vacancy, zinc vacancy, oxygen interstitial, and zinc interstitial or surface-related states [18]. It is noted that the UV emission intensity of ZnO/MgO core–shell nanorods is about 32 times higher than the as-prepared ZnO nanorods. Generally, ZnO grown in the chemical solution has two kinds of defects, i.e., surface defects and intrinsic defects. Since the intensities of DLE bands for both spectra are almost same as shown in Fig. 4, indicating the intrinsic defect concentration for both samples are similar, which is reasonable because the ZnO/MgO were directly converted from ZnO nanorods. Therefore, the strong enhancement of UV emission of ZnO/MgO nanorods is mainly attributed to the strong suppression of surface defects due to the deposition of MgO shell. The

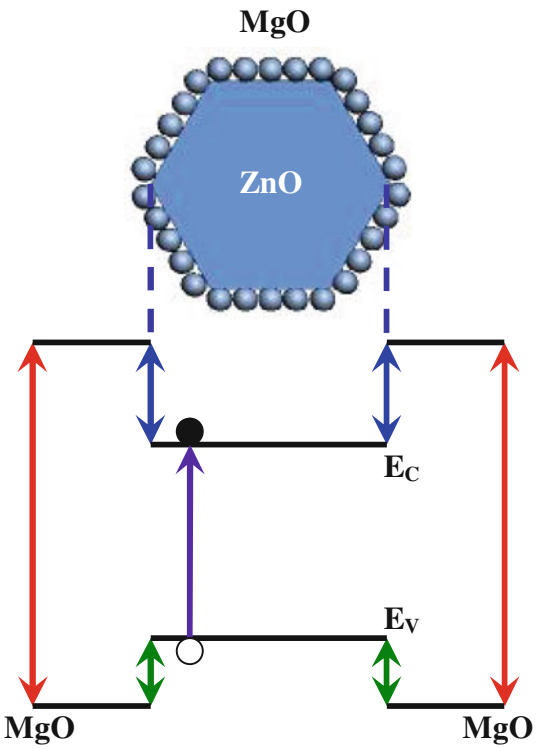

Fig. 6 Schematic energy band diagram of ZnO/MgO heterojunction. A type-I band heterojunction is formed in the staggered arrangement

existence of MgO layer can effectively suppress the nonradiative recombination on the surface of the ZnO nanorods, resulting in the enhancement of excitonic radiative recombination at UV wavelength [19]. Similar improvement in UV emission intensity has also been reported in ZnO nanorods covered with dielectric shells [20].

Figure 5 shows the PL spectra obtained at 80 K for the initial ZnO nanorods and ZnO/MgO core–shell nanorods. The lines located at 3.368, 3.356, 3.308 eV can be ascribed to the FX, D^0X, and A^0X emission, respectively, which are quite agreeable with other research results [21]. The rest of the lines are LO phonon replicas, separated by 71–73 meV, which are associated with free and bound excitons [22]. In comparison to the as-prepared ZnO nanorods, MgO coating caused blue shift in the FX, D^0X, A^0X, and A^0X-LO emissions. In general, the core/shell structures are typically classified into two types according to the band alignment of the two components. Type-I, the conduction band minimum (CBM) of the shell is of higher energy than that of the core, and the valence band maximum (VBM) of the shell is of lower energy than that of the core, which provides the lowest energy states for both electrons and holes. Type-II, both the valence and conduction bands in the core are lower (or higher) than that in the shell; therefore, the energy gradient existing at the interfaces tends to spatially separate electrons and holes on different sides of the heterojunction [23, 24]. As shown in Fig. 6, ZnO/MgO core–shell nanorod arrays belong to type-I, which will lead to the peak blue shift and improve UV emission intensity compared with ZnO nanorods.

Figure 7 shows the temperature-dependent PL spectra of the as-prepared ZnO nanorods and ZnO/MgO core–shell nanorods from 78 to 298 K. As shown in Fig. 7a, the PL spectra of the as-prepared ZnO nanorods exhibit several resolved NBE emissions at low temperatures. For the spectra of the ZnO/MgO core–shell nanorods (Fig. 7b), the free exciton (FX), neutral donor exciton (D^0X), neutral acceptor exciton (A^0X), and longitudinal optic (LO) phono replica emissions are observed. PL transition intensities of two samples drastically decrease with increasing temperature. But the intensity quenching behaviors of two samples are quite different. Figure 7c shows the integrated intensity of PL as a function of temperature for the two samples. The observed overall temperature-quenching behavior can be well described by the equation $I(T) = I_0/[1 + A\exp(-E_a/k_BT)]$ [25], where $I(T)$ and I_0 are the PL intensities at temperature T and 0 K, A is the process rate parameter, k_B is the Boltzmann constant, and E_a is the activation energy in the thermal quenching process. The best fit result is shown by the dotted curve in Fig. 7c. The good fits (solid curves) yielded E_a of 23 and 63 meV for the as-prepared ZnO nanorods and ZnO/MgO core–shell nanorods, respectively. Lin et al. point out that the lower activation energy is mainly due to the existence of more nonradiative contributions in the materials, which also can be deduced from the equation [26]. Therefore, we can conclude that more nonradiative recombination contribute to the emission process in the as-prepared ZnO nanorods than that in ZnO/MgO core–shell nanorods. This is also consistent with the results shown earlier [27], and stronger PL intensity in ZnO/MgO core–shell nanorods in comparison with the as-prepared ZnO nanorods.

4 Conclusion

In summary, we presented the synthesis, structural, and optical properties of ZnO/MgO core–shell nanorod arrays. The PL intensity of ZnO/MgO core–shell nanorod arrays increased 32-fold, after introduction of MgO overcoating onto bare ZnO cores. MgO layer suppresses the nonradiative recombination on the surface of the ZnO nanorods and its type-I structure results in the high UV emission intensity. The improved UV emission performance and the simple fabrication technique suggest that the ZnO/MgO core–shell nanorod arrays may serve as good UV laser devices.

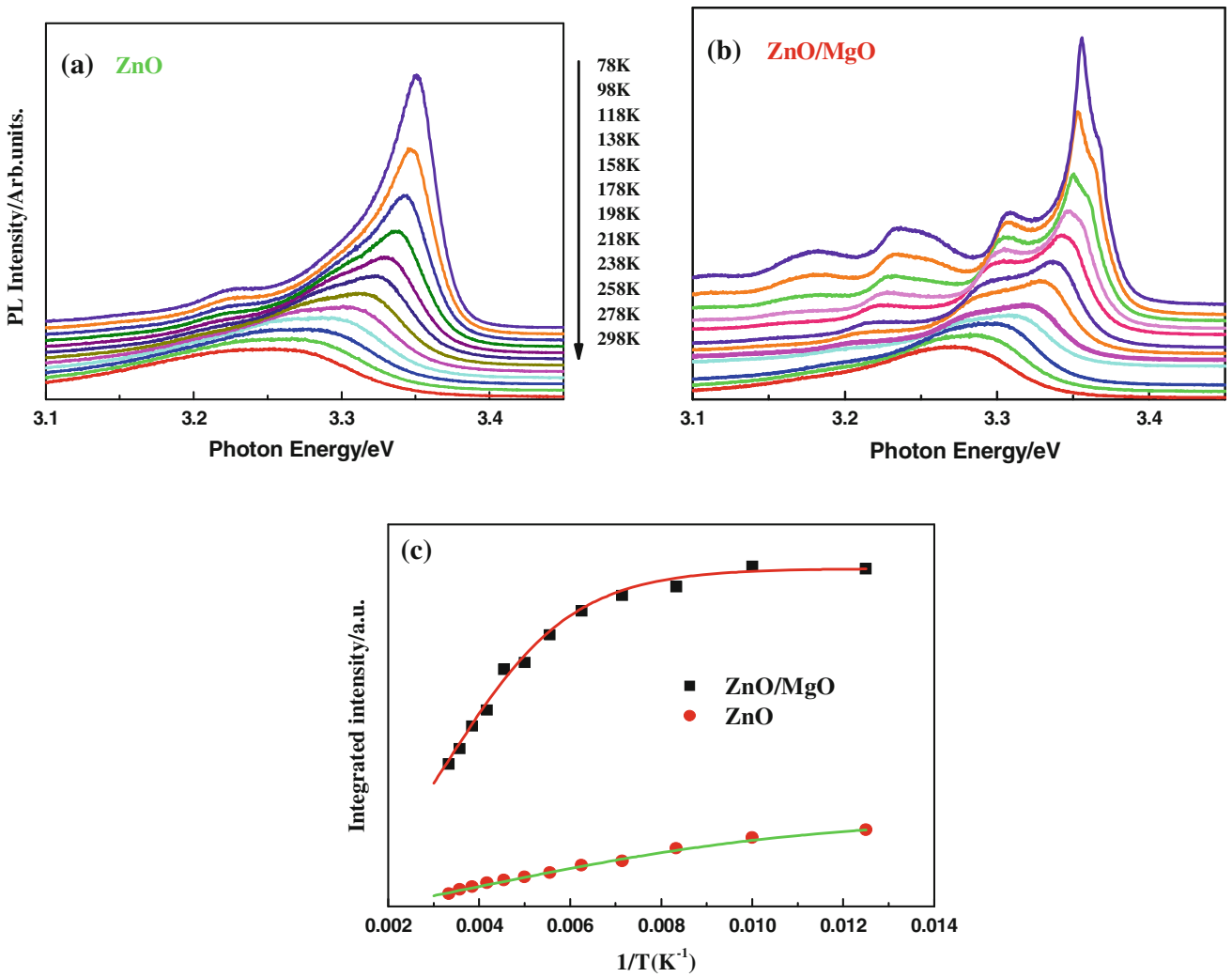

Fig. 7 PL spectra of **a** the initial ZnO nanorods in a temperature range from 80 to 300 K; **b** ZnO/MgO core–shell nanorod arrays in a temperature range from 80 to 300 K; **c** reciprocal temperature-dependent entire intensities of the initial ZnO nanorods and ZnO/MgO core–shell nanorod arrays. The *solid lines* in the figure are the result of simulation

Acknowledgments This work is supported by Program for the National Natural Science Foundation of China (Grant Nos. 61008051, 61178074), Program for the development of Science and Technology of Jilin province (Item Nos. 201215225, 201105084, 201205078 and 201215223).

References

1. D.C. Olson, J. Piris, R.T. Collins, S.E. Shaheen, D.S. Ginley, Thin Solid Films **496**, 26 (2006)
2. Y. Ryu, T.S. Lee, J.A. Lubguban, H.W. White, B.J. Kim, Y.S. Park, C.J. Youn, Appl. Phys. Lett. **88**, 241108 (2006)
3. B. Sun, H. Sirringhaus, Nano Lett. **5**, 2408 (2005)
4. Y. Liu, Y. Chu, L.L. Li, L.H. Dong, Y.J. Zhuo, Chem. Eur. J. **13**, 6667 (2007)
5. H.S. Chung, C.S.H. Chen, R.A. Kremer, J.R. Boulton, G.W. Burdette, Energy Fuels **13**, 641 (1999)
6. L. Vayssieres, Adv. Mater. **15**, 464 (2003)
7. Q. Li, V. Kumar, Y. Li, H. Zhang, T.J. Marks, R.P.H. Chang, Chem. Mater. **17**, 1001 (2005)
8. L. Schmidt-Mende, J.L. MacManus-Driscoll, Today **10**, 40 (2007)
9. S. Kim, C.O. Kim, S.W. Hwang, S.H. Choi, Appl. Phys. Lett. **92**, 243108 (2008)
10. S.S. Lee, K.T. Byun, J.P. Park, S.K. Kim, J.C. Lee, S.K. Chang, H.Y. Kwak, I.W. Shim, Chem. Eng. J. **139**, 194 (2008)
11. J.C. Jiang, E.I. Meletis, Z. Yuan, C.L. Chen, Appl. Phys. Lett. **90**, 051904 (2007)
12. G.W. Wagner, P.W. Bartram, O. Kopper, K.J. Klabunde, J. Phys. Chem. B **103**, 3225 (1999)
13. O.A. Boateng, S.K. Aska Kumarao, M. Okuya, K. Murakami, A. Konno, K. Tennakone, J. Appl. Phys. **44**, 731 (2005)
14. J.H. Yang, J.H. Lang, L.L. Yang, Y.J. Zhang, D.D. Wang, H.G. Fan, H.L. Liu, Y.X. Wang, M. Gao, J. Alloys Compd. **450**, 521 (2008)
15. T.C. Damen, S.P.S. Porto, B. Tell, Phys. Re. **142**, 570 (1966)
16. A. Kaschner, U. Haboeck, M. Strassburg, G. Kaczmarczyk, A. Hoffmann, C. Thomsen, A. Zeuner, H.R. Alves, D.M. Hofmann, B.K. Meyer, Appl. Phys. Lett. **80**, 1909 (2002)
17. X.H. Wang, D.X. Zhao, Y.C. Liu, J.Y. Zhang, Y.M. Lu, X.W. Fan, J. Cryst. Growth **263**, 316 (2004)

18. K. Vandheusen, W.L. Warren, C.H. Seager, D.R. Tallant, J.A. Voigt, B.N. Gnage, J. Appl. Phys. **79**, 7983 (1996)
19. H.Y. Yang, S.F. Yu, G.P. Li, T. Wu, Opt. Lett. **18**, 13647 (2010)
20. J.H. Li, D.X. Zhao, X.Q. Meng, Z.Z. Zhang, J.Y. Zhang, D.Z. Shen, Y.M. Lu, X.W. Fan, J. Phys. Chem. B **110**, 14685 (2006)
21. V.A. Fonoberov, K.A. Alim, A.A. Balandin, Phys. Rev. B **73**, 165317 (2006)
22. J. Li, L.W. Wang, Chem. Mater. **16**, 4012 (2004)
23. S. Kim, B. Fisher, H.J. Eiser, M.J. Bawendi, Am. Chem. Soc. **125**, 11466 (2003)
24. S. Kumar, M. Jones, S.S. Lo, G.D. Scholes, Small **3**, 1633 (2007)
25. S.A. Ivanov, A. Piryatinski, J. Nanda, S. Tretaik, K.R. Zavadil, W.O. Wallace, D. Werder, V.I. Klimov, J. Am. Chem. Soc. **129**, 11708 (2007)
26. X.Q. Meng, H.W. Peng, Y.Q. Gai, J.B. Li, J. Phys. Chem. C **114**, 1467 (2010)
27. L.L. Yang, Q.X. Zhao, M.Q. Israr, J.R. Sadaf, M. Willander, G. Pozina, J.H. Yang, J. Appl. Phys. **108**, 103513 (2010)